Including higher harmonics in gravitational-wave parameter estimation and cosmological implications for LISA

Yi Gong,[1,2,3] Zhoujian Cao,[4,1,5] Junjie Zhao,[4,1,*] and Lijing Shao[6,7]

[1]*Department of Astronomy, Beijing Normal University, Beijing 100875, China*
[2]*School of Physics and Technology, Wuhan University, Wuhan, Hubei 430072, China*
[3]*Institute for Cosmic Ray Research (ICRR), KAGRA Observatory, The University of Tokyo, Kashiwa 277-8582, Japan*
[4]*Institute for Frontiers in Astronomy and Astrophysics, Beijing Normal University, Beijing 102206, China*
[5]*School of Fundamental Physics and Mathematical Sciences, Hangzhou Institute for Advanced Study, UCAS, Hangzhou 310024, China*
[6]*Kavli Institute for Astronomy and Astrophysics, Peking University, Beijing 100871, China*
[7]*National Astronomical Observatories, Chinese Academy of Sciences, Beijing 100012, China*

(Received 12 April 2023; accepted 25 August 2023; published 25 September 2023)

Massive black holes (MBHs) are crucial in shaping their host galaxies. How the MBH co-evolves with its host galaxy is a pressing problem in astrophysics and cosmology. The valuable information carried by the binary MBH is encoded in the gravitational waves (GWs), which will be detectable by the space-borne GW detector LISA. In the GW data analysis, usually only the dominant (2,2) mode of the GW signal is considered in the parameter estimation for LISA. However, including the higher harmonics in parameter estimation can break the degeneracy between the parameters, especially for the inclination angle and luminosity distance. This may enable the identification of GW signals without electromagnetic counterparts, known as "dark sirens." Thus, incorporating higher harmonics will be beneficial to resolve the Hubble tension and constrain the cosmological model. In this paper, we investigate the role of higher harmonics in the parameter estimation for GWs emitted by binary MBHs. We demonstrate that including the (3,3) mode can lead to a 10^3-times improvement in angular resolution and a 10^4-times improvement in luminosity distance. Meanwhile, our results indicate that considering higher harmonics increases the probability of identifying over 70% host galaxies from 10^{-2} Gpc^3 cosmological volume threshold (corresponding 10^5 host galaxies), while the probability is less than 8% for only the (2,2) mode. Thus, our results underscore the importance of including higher modes in the GW signal from binary MBHs, for LISA at least (3,3) mode.

DOI: 10.1103/PhysRevD.108.064046

I. INTRODUCTION

Properties of massive ($\sim 10^4$–$10^8 M_\odot$) black holes (MBHs) are crucial to understanding the evolution of their hosts [1–3] and are relevant to open problems in astrophysics and cosmology, such as dark matter, vacuum energy, and the early Universe [4]. Gravitational waves (GWs) provide a valuable tool for constraining the Hubble constant (H_0), referred to as "sirens," by inferring distance directly from the signals, and the redshift z is from the host galaxy or the electromagnetic (EM) counterpart [5,6].

The Laser Interferometer Space Antenna (LISA), a space-borne GW detector building on the success of LISA Pathfinder and other ground-based detectors, will target these GW sources from tens of microhertz up to decihertz [7–9]. By observing these sources, LISA will provide insights into the evolution of MBHs from the early Universe through to the peak of the star formation era, offering key information for future studies in astrophysics and cosmology.

LISA is sensitive to a different frequency band compared to existing ground-based detectors, such as the Laser Interferometer GW Observatory (LIGO) [10], Virgo [11], and KAGRA [12]. Signals from MBHs will last several months to years in the lifetime of LISA, which will lead to signal modulation effects as LISA changes its orientation and position during observations [9,13]. The signal-to-noise ratio (SNR), a measure of the strength of the signal relative to the noise, of the signal detected by ground-based detectors is typically $\mathcal{O}(10)$ at present [14–17]. However, signals from MBHs detected by LISA will have much higher SNRs of $\mathcal{O}(10^3)$ [13,18], almost 100-fold louder. It makes LISA an invaluable tool for studying these elusive sources of GWs and opens up new opportunities for insights into their properties and evolution.

The signal modulation effect caused by LISA motion will break the parameter degeneration, resulting in a high-precision source parameter extraction. Incorporating higher

*junjiezhao@bnu.edu.cn

harmonics into GW data analysis will further break the parameter degeneration, which may lead to a higher precision parameter extraction. For GWs emitted by compact binary coalescences (CBCs), the waveform can be expressed as a linear superposition of spin-weighted spherical harmonic functions and the waveform component of each harmonic [19,20]. The dominant mode of the GW signal is the $(\ell, |m|) = (2, 2)$ mode. Subdominant harmonics such as $(\ell, |m|) = (3, 3)$, (4,4), or (2,1) can usually have amplitudes up to ∼10% of the dominant mode [21]. However, the subdominant harmonics are usually ignored in the data analysis for LISA.

Incorporating higher harmonics into GW data analysis has become increasingly important in recent years. There are several binary black hole (BBH) events detected by GW observatories that show evidence of higher harmonics. Notably, GW190412 [22] is the first event with significant evidence for higher harmonics, featuring a mass ratio of approximately 3.57 and a total SNR of about 19. The $(\ell, |m|) = (3, 3)$ harmonic mode contributes about 3 to the SNR. Another event, GW190814 [23], also shows evidence of the $(\ell, |m|) = (3, 3)$ harmonic mode, with a mass ratio of approximately 8.93 and a total SNR of about 25. This event is particularly asymmetric in masses. These two events, along with GW170729 (slightly weaker evidence) [14,24], point towards the potential for higher harmonics to improve parameter estimation. This means that these higher harmonics can be detectable in GW signals with large SNRs, and their inclusion in waveform models can improve parameter estimation. Because of the high SNR of LISA data, higher harmonics are indispensable in LISA data analysis.

Higher harmonics are essential for accurately estimating orbit precession [25], and can also help to constrain alternative gravity theories [26,27]. Ignoring higher harmonics can lead to significant systematic errors in parameter estimation [28,29]. Several recent studies have investigated the effects of including higher harmonics on LISA parameter estimation. When considering the inspiral phase, using higher post-Newtonian (PN) orders that include higher harmonics can improve LISA angular resolution by a factor of about 10^2 [30–32]. Higher harmonics of the ringdown phase may be detected by LISA through analysis of the ringdown waveform, and subdominant harmonics play a critical role in source localization [33]. When analyzing full waveforms, incorporating higher harmonics can improve the precision of luminosity distance estimation by a factor of around 50 [26], and sky angular resolution by a factor of approximately 10^3 in certain specific systems [34,35]. Many other recent studies also support the conclusion that including higher harmonics can improve parameter estimation [36–38].

The precision of localization and distance inference is a crucial factor to achieve a high-precision H_0 measurement. However, EM counterparts to GW events are much rarer than events without counterparts, which would lead to poor localization. To date, only one GW event, GW170817, has provided a H_0 measurement using an EM counterpart [39–43]. Because of the degeneracy between the luminosity distance and the inclination angle, the measurement of H_0 from GW170817 is not good enough. The GW measurement is broadly consistent with the results from Plank [44] and SH0ES [45] Collaborations, while these two results are inconsistent at the $\geq 3\sigma$ level. GWs without EM counterparts, referred to as "dark sirens," can also be used to constrain H_0 in a statistical way [46–50], but the constraint on H_0 is limited by the uncertainty in the source location. Incorporating higher harmonics into data analysis is promising to resolve this conundrum. The considerable improvement in localization and distance inference provided by GWs makes them a more powerful tool for investigating cosmology by locating the host galaxy and a promising avenue for resolving the existing H_0 tension problem [44,45].

Recently, Yang *et al.* [51] found GWs emitted by the eccentric compact binaries in the decihertz band can significantly improve the angular resolution, potentially leading to new opportunities for probing cosmology. However, the question of the probability of achieving such a dramatic improvement in the source location—a crucial factor for studying H_0 and cosmology—remains unanswered.

In this paper, we investigate how the parameters such as binary masses, source location, and higher harmonics impact LISA parameter estimation. When considering a face-on or face-off MBH binary with the total mass of $\sim 10^6 M_\odot$, we find the varying mass ratio only lightly impacts the parameter extraction. Meanwhile, including higher harmonics will significantly enhance the precision of luminosity distance and angular resolution by a factor of 10^4 and 10^3, respectively. In the meantime, higher harmonics will improve the ability to localize the host galaxies of MBH binaries, compared to only involving the (2,2) mode. For instance, if the threshold volume is 10^{-2} Gpc (excepted number of host galaxies within this volume is 10^5), including the (3,3) mode will increase this probability from less than 8% to 70%. Thus, our results suggest including higher modes for LISA data analysis, at least the (3,3) mode.

The rest of this paper is organized as follows. In Sec. II, we review the GW waveform including higher harmonics. Meanwhile, we also review the Fisher matrix method to estimate the measurement precision. In Sec. III, we exhibit the effect caused by higher harmonics. In Sec. IV, we make a summary of our work and provide some concluding remarks. The geometrized units $G = c = 1$ are used throughout this paper.

II. GRAVITATIONAL WAVES DETECTED BY LISA

The frequency-domain GW strain $\tilde{h}(f)$ measured by LISA is [13,52]

$$\tilde{h}(f) = \frac{\sqrt{3}}{2}(F^{+}(f)\tilde{h}_{+}(f) + F^{\times}(f)\tilde{h}_{\times}(f))e^{-i\phi_D(f)}, \quad (1)$$

where $\tilde{h}_{+}(f)$ and $\tilde{h}_{\times}(f)$ are two orthogonal polarizations of GWs, "plus" and "cross" modes in the transverse-traceless gauge; $F^{+}(f)$ and $F^{\times}(f)$ are the pattern functions of the detector and there is a factor $\frac{\sqrt{3}}{2}$ because of the equilateral triangle shape. $\phi_D(f)$ is the Doppler effect phase caused by LISA motion [see Eq. (7)].

In this paper, we employ the IMRPhenomHM [21] waveform template to generate $\tilde{h}_{+}(f), \tilde{h}_{\times}(f)$. IMRPhenomHM is an inspiral-merger-ringdown waveform with the higher harmonics $(\ell, |m|) = (3,3), (4,4), (3,2), (2,1), (4,3)$. For simplicity, we only consider the nonspinning BBHs with seven physical parameters to generate the waveform template. They are the source-frame component masses m_1 and m_2, the inclination angle ι, the reference orbit phase ϕ_0, the time to coalescence t_c, the luminosity distance $D_{\rm L}$, and the corresponding cosmological redshift z. The binaries' chirp mass $\mathcal{M}$ and symmetric mass ratio η are defined as

$$\eta = m_1 m_2 / M^2, \quad (2a)$$

$$\mathcal{M} = \eta^{3/5} M. \quad (2b)$$

Here $M = m_1 + m_2$ is the total mass of the binary, and the mass ratio is $q \equiv m_1/m_2 \geq 1$.

Moreover, we use the Λ cold dark matter cosmology model to obtain the luminosity distance $D_{\rm L}$ from the redshift z,

$$D_{\rm L}(z) = \frac{1+z}{H_0}\int_0^z \frac{dz'}{\sqrt{\Omega_\Lambda + \Omega_{\rm m}(1+z')^3}}. \quad (3)$$

Here, we take this cosmology model with the Hubble constant $H_0 = 67.4\ {\rm km\,s^{-1}\,Mpc^{-1}}$, the matter density parameter $\Omega_{\rm m} = 0.315$, and the dark energy density parameter $\Omega_\Lambda = 0.685$ [44].

In this paper, we fix all the BBH sources located at $z = 1$ for illustration.

A. LISA pattern functions

The pattern functions depend on the sky location in the detector frame $(\hat{\theta}_S, \hat{\phi}_S)$ and the polarization angle of GWs $(\hat{\psi})$ of the GW source [13],

$$F_A^{+}(\hat{\theta}_S, \hat{\phi}_S, \hat{\psi}) = \frac{1}{2}(1+\cos^2\hat{\theta}_S)\cos 2\hat{\phi}_S \cos 2\hat{\psi} - \cos\hat{\theta}_S \sin 2\hat{\phi}_S \sin 2\hat{\psi}, \quad (4a)$$

$$F_A^{\times}(\hat{\theta}_S, \hat{\phi}_S, \hat{\psi}) = \frac{1}{2}(1+\cos^2\hat{\theta}_S)\cos 2\hat{\phi}_S \sin 2\hat{\psi} + \cos\hat{\theta}_S \sin 2\hat{\phi}_S \cos 2\hat{\psi}, \quad (4b)$$

$$F_B^{+}(\hat{\theta}_S, \hat{\phi}_S, \hat{\psi}) = F_A^{+}(\hat{\theta}_S, \hat{\phi}_S - \pi/4, \hat{\psi}), \quad (4c)$$

$$F_B^{\times}(\hat{\theta}_S, \hat{\phi}_S, \hat{\psi}) = F_A^{\times}(\hat{\theta}_S, \hat{\phi}_S - \pi/4, \hat{\psi}). \quad (4d)$$

Here, a triangle GW detector like LISA can be equivalent to two L-shaped detectors like LIGO denoted as detectors "A" and "B." The "hatted" coordinate implies it is tied to the LISA's detector frame while the "unhatted" one is tied to the ecliptic frame. The unit vector of the GWs propagation direction $\boldsymbol{N}$ and unit vector of CBCs orbital angle momentum $\boldsymbol{L}$ can be described by (θ_S, ϕ_S) and (θ_L, ϕ_L) in the ecliptic frame, respectively. Following the method in Ref. [13], we can relate $\{\hat{\theta}_S, \hat{\phi}_S, \hat{\psi}\}$ in Eq. (4) to the ecliptic coordinates $\{\theta_S, \phi_S, \theta_L, \phi_L\}$ through the following:

$$\cos\hat{\theta}_S = \frac{1}{2}\cos\theta_S - \frac{\sqrt{3}}{2}\sin\theta_S\cos\bar{\phi}_S, \quad (5a)$$

$$\hat{\phi}_S = \frac{2\pi t}{T} - \frac{\pi}{12} + \tan^{-1}\left(\frac{\sqrt{3}\cos\theta_S + \sin\theta_S\cos\bar{\phi}_S}{2\sin\theta_S\sin\bar{\phi}_S}\right), \quad (5b)$$

$$\tan\hat{\psi} = \frac{\hat{\boldsymbol{z}}\cdot\boldsymbol{p}}{\hat{\boldsymbol{z}}\cdot\boldsymbol{q}}, \quad (5c)$$

$$\boldsymbol{L} = (\sin\theta_L\cos\phi_L, \sin\theta_L\sin\phi_L, \cos\theta_L), \quad (5d)$$

$$\boldsymbol{N} = (\sin\theta_S\cos\phi_S, \sin\theta_S\sin\phi_S, \cos\theta_S), \quad (5e)$$

$$\hat{\boldsymbol{z}} = \left(-\frac{\sqrt{3}}{2}\cos\bar{\phi}, -\frac{\sqrt{3}}{2}\sin\bar{\phi}, \frac{1}{2}\right), \quad (5f)$$

where $\hat{\boldsymbol{z}}$ is the unit vector in the $\hat{z}$ direction, $\bar{\phi}_S = \bar{\phi} - \phi_S$, and $\bar{\phi} = 2\pi t/T$ is the coordinate of the detector at time t with the LISA orbit period $T = 1$ yr.

For a GW signal, we can obtain $t(f)$ from the GW phase evolution $\Phi(f)$ at 0PN order approximately [53]

$$t(f) = \frac{1}{2\pi}\frac{d\Phi(f)}{df} = t_c - 5(8\pi f)^{-8/3}\mathcal{M}^{-5/3}. \quad (6)$$

Note that this relation is derived from the inspiral stage with the stationary phase approximation [53]. However, this is still a good approximation for the entire stage of GW due to the rapid evolution during the merger and ringdown stages.

Space-borne GW detector LISA moves along an orbit that lays on the Sun's equator during the observation period, so there is a phase modulation in the signal, the so-called Doppler phase ϕ_D,

$$\phi_D(t) = 2\pi f R\sin\theta_S\cos[\bar{\phi}(t) - \phi_S], \quad (7)$$

where $R = 1$ au is the distance between LISA and the Sun. We can easily combine $\phi_D(t)$ and Eq. (6) to obtain $\phi_D(f)$

in Eq. (1). In addition, we can also obtain the inclination angle ι by

$$\cos\iota = \boldsymbol{L}\cdot\boldsymbol{N}. \tag{8}$$

B. Higher harmonic waveforms

The time-domain plus and cross components $h_+(t)$ and $h_\times(t)$ can be decomposed into higher harmonics [20,54]:

$$h_+(t) - \mathrm{i}h_\times(t) = \sum_{\ell,m} {}_{-2}Y_{\ell m}(\iota,\phi_0)h_{\ell m}(t;\mathcal{M},\eta,D_\mathrm{L},t_c), \tag{9}$$

$${}_{-2}Y_{\ell m}(\iota,\phi_0) = \sqrt{\frac{2\ell+1}{4\pi}} d^{\ell m}_{-2}(\iota)e^{\mathrm{i}m\phi_0}. \tag{10}$$

Here, ${}_{-2}Y_{\ell m}(\iota,\phi_0)$ is spin-weighted spherical harmonic function with weight -2, and $d^{\ell m}_{-2}$ is a specific of Wigner d function, $\ell \geq 2$ and $|m| \leq \ell$, leading to significant contributions for different harmonics. Here, we illustrate the amplitude ratio of ${}_{-2}Y_{\ell m}(\iota,\phi_0)$ relative to that of $(\ell,m) = (2,2)$ in Fig. 1. When considering a face-on or face-off $(\iota = 0,\pi)$ CBC, there are only two harmonics $(\ell,m) = (2,2)$ and (3,2) included in the waveform. For an edge-on $(\iota = \pi/2)$ system, the relative contributions from higher harmonics are large.

The frequency domain waveforms $\tilde{h}_+(f)$ and $\tilde{h}_\times(f)$ can be obtained from the time-domain GW strain by Fourier transform,

$$\tilde{h}_{+,\times}(f) = \int_{-\infty}^{\infty} h_{+,\times}(t)e^{2\pi\mathrm{i}ft}\mathrm{d}t. \tag{11}$$

Since $h_+(t)$ and $h_\times(t)$ are real functions of time, from Eq. (9) we can show that

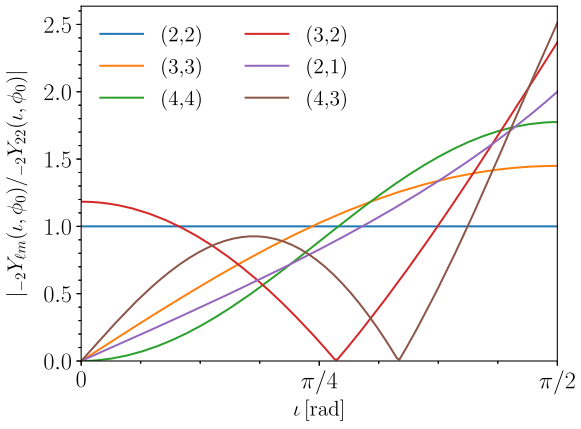

FIG. 1. The amplitude ratio of the spin-weighted spherical harmonic to ${}_{-2}Y_{22}(\iota,\phi_0)$, where $\phi_0 = 0$. Each line corresponds to a different harmonic mode.

$$h_+ = \frac{1}{2}\sum_{\ell,m}[{}_{-2}Y_{\ell m}(\iota,\phi_0)h_{\ell m} + {}_{-2}Y^*_{\ell m}(\iota,\phi_0)h^*_{\ell m}], \tag{12a}$$

$$h_\times = \frac{\mathrm{i}}{2}\sum_{\ell,m}[{}_{-2}Y_{\ell m}(\iota,\phi_0)h_{\ell m} - {}_{-2}Y^*_{\ell m}(\iota,\phi_0)h^*_{\ell m}]. \tag{12b}$$

For a nonprecessing BBH, there exists a useful symmetry property for higher harmonics: $h^*_{\ell m}(t) = (-1)^\ell h_{\ell,-m}(t)$. With the symmetry property of time-domain waveforms and by performing Fourier transform, we can obtain

$$\tilde{h}_{+,\times}(f) = \sum_{\ell m}\mathcal{Y}^{+,\times}_{\ell m}\tilde{h}_{\ell m}(f), \tag{13}$$

where

$$\mathcal{Y}^{+}_{\ell m} = \frac{1}{2}[{}_{-2}Y_{\ell m}(\iota,\phi_0) + (-1)^\ell {}_{-2}Y^*_{\ell,-m}(\iota,\phi_0)], \tag{14a}$$

$$\mathcal{Y}^{\times}_{\ell m} = \frac{\mathrm{i}}{2}[{}_{-2}Y_{\ell m}(\iota,\phi_0) - (-1)^\ell {}_{-2}Y^*_{\ell,-m}(\iota,\phi_0)]. \tag{14b}$$

Based on the discussion in Sec. II A and this section, nine parameters can characterize the GW signal in LISA. We list them in Table I, with $\mu_S \equiv \cos\theta_S$ and $\mu_L \equiv \cos\theta_L$. The parameters' range means the value used in this investigation. And for convenience, we use the notation in Table II to indicate which harmonics are used.

We investigate the characteristic strain for the two BBH systems and compare the individual harmonics strain and the total strain. Figure 2 shows the each harmonics of GWs with $M = 10^4 M_\odot$ and $M = 10^8 M_\odot$. We can find that when M is relatively small, only (3,3) and (4,4) modes are significant. But when M is relatively large, more higher-order modes are visible, and the effect may not be neglected. It is mainly because the higher-order modes contribute more to the strain amplitude in the merger and

TABLE I. Parameters that characterize the GW signal. Here, we fix the redshift $z = 1$ and the luminosity distance $D_\mathrm{L} = 6791.27$ Mpc. The direction of sources' angular momentum is fixed to be $(\mu_L,\phi_L) = (0.3, 2.0)$. The time to coalescence $t_c = 0$ and $\phi_0 = 0$.

Notation	Range	Unit
μ_S	$[-1,1]$	1
μ_L	0.3	1
ϕ_S	$[0,2\pi]$	rad
ϕ_L	2.0	rad
$\mathcal{M}$	$[\mathcal{M}_\mathrm{min},\mathcal{M}_\mathrm{max}]$	$M_\odot$
η	$[\eta_\mathrm{min},\eta_\mathrm{max}]$	1
D_L	6791.27	Mpc
t_c	0	s
ϕ_0	0	rad

TABLE II. Different scenarios for investigating the effects from higher harmonics in data analysis for LISA.

Notation	$(\ell, \lvert m\rvert)$
I	(2,2)
II	(2,2), (3,3)
III	(2,2), (3,3), (4,4)
IV	(2,2), (3,3), (4,4), (3,2)
V	(2,2), (3,3), (4,4), (3,2), (2,1)
VI	(2,2), (3,3), (4,4), (3,2), (2,1), (4,3)

ringdown stages. For the space-borne GW detector LISA, MBH binary systems need to include higher modes to extract more information from the observed data.

C. SNRs

We adopt the matched-filtering method [55] to estimate the SNR of GWs. For a given GW strain $\tilde{h}(f)$, the optimal SNR is defined as

$$\rho \equiv (\tilde{h}(f)|\tilde{h}(f))^{1/2}, \tag{15}$$

where operator $(\tilde{\mathcal{A}}|\tilde{\mathcal{B}})$ is the noise-weighted inner product between two signals $\tilde{\mathcal{A}}(f)$ and $\tilde{\mathcal{B}}(f)$,

$$(\tilde{\mathcal{A}}|\tilde{\mathcal{B}}) = 2\int_{f_{\rm low}}^{f_{\rm high}} \frac{\tilde{\mathcal{A}}(f)\tilde{\mathcal{B}}^*(f) + \tilde{\mathcal{A}}^*(f)\tilde{\mathcal{B}}(f)}{S_n(f)} \mathrm{d}f. \tag{16}$$

In this paper, we set $f_{\rm high} = 1$ Hz for LISA and deduce $f_{\rm low}$ by

$$f_{\rm low} = \left(\frac{(8\pi)^{8/3} T_{\rm obs}}{5\mathcal{M}^{5/3}} - f_{\rm high}^{-8/3}\right)^{-3/8}. \tag{17}$$

$S_n(f)$ is the one-sided power spectrum density of noise. We adopt the LISA sensitivity curves in Ref. [56], with $L = 2.5 \times 10^9$ m as the arm length of LISA, and an observation span $T_{\rm obs} = 4$ yr.

From Fig. 2, we show the effect of higher harmonics relating to the total mass M. The corresponding SNRs are illustrated in Fig. 3, which the sources located at $z = 1$, the total mass M varies from $10^4 M_\odot$ to $10^8 M_\odot$, and the other parameters of the sources are $q = 10$, $\mu_S = -0.25$, $\phi_S = 2.31$, $\mu_L = 0.3$, $\phi_L = 2.0$, $\phi_0 = 0$, and $t_c = 0$ s. The deviations between the (2,2) mode and other scenarios increase as M increases, as implied in Fig. 2. Meanwhile, our analysis indicates that LISA is most sensitive to $M \sim 10^6 M_\odot$, and SNRs exhibit oscillatory behavior as M increases. This is due to SNRs being the inner product of $h(f)$ with itself, where $h(f)$ is a linear superposition of each harmonic. The cross term of different harmonics can cause constructive or destructive interference, which has been noted by Marsat *et al.* [34] and Mills and Fairhurst [57]. So in

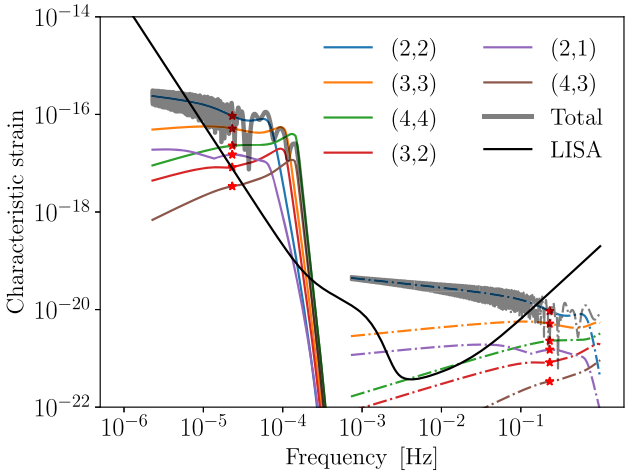

FIG. 2. The characteristic strains $2f|\tilde{h}_+(f)|$ of different BBHs in the LISA 4-yr observation. We set their physical parameters $q = 10, \iota = \pi/2, z = 1$ with total mass $M = 10^8 M_\odot$ (solid lines) and $M = 10^4 M_\odot$ (dashed lines). The solid black line in the figure is the characteristic strain of the detector noise, $\sqrt{fS_n(f)}$. Each colored line represents a single harmonic component of GWs. Red stars denote the innermost stable circular orbit frequency, and the thick gray line is the total strain of all harmonics in the figure.

Fig. 3, the SNRs curve is smooth when only involving the (2,2) mode and oscillations appear when higher harmonics are involved. Additionally, with respect to the relatively small mass source, compared with the (2,2) mode, the effect of higher harmonics is not so significant (see Fig. 2);

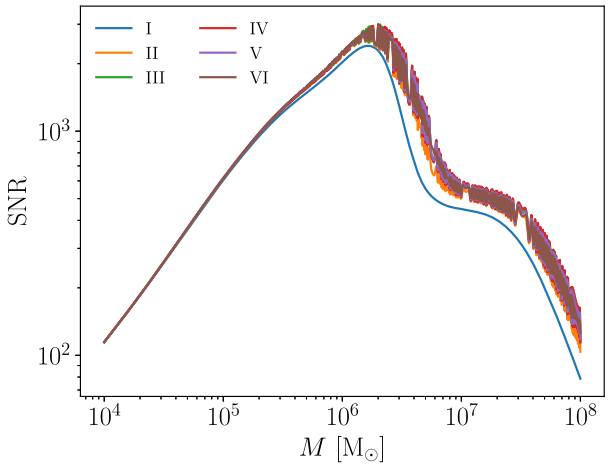

FIG. 3. The SNRs as a function of total mass M. The sources are located at $z = 1$, mass ratio $q = 10$, $\phi_0 = 0$, $t_c = 0$ s, and angular parameters $(\mu_S, \phi_S, \mu_L, \phi_L) = (-0.25, 2.31, 0.3, 2.0)$. Each curve corresponds to a different scenario and adopts the same notation as Table II. Since the SNRs of the different scenarios are close, several curves overlap. With the increasing M, the oscillation increases, which means the effect of higher harmonics increases.

therefore, the oscillatory behavior is not notable for the scenarios which incorporate higher harmonics.

Besides, we also investigate the effect of varying mass ratio q in Fig. 4. The sources' parameters are the same as Fig. 3 except total mass $M = 1.1 \times 10^6 M_\odot$, and the mass ratio q varies from 2 to 10. The oscillations also result from constructive or destructive interference of different harmonics, the same as Fig. 3. As expected, the SNR deviation between different scenarios becomes more significant as q increases, as the BBH becomes more asymmetric. When the total mass is fixed, a larger q leads to a smaller SNR, which is related to a smaller $\mathcal{M}$. In other words, Figs. 3 and 4 imply that higher harmonics are more significant for a heavier and asymmetric BBH. Moreover, the oscillations that appear in Figs. 3 and 4 will reappear in the subsequent parameter estimation for the same reason.

In Fig. 1, we show that the higher harmonics strongly depend on the inclination angle ι, i.e., the BBH orbital angular momentum and location. Thus, investigating the effect of location is promising. To visualize the inclination angle ι, we fix $\mu_L = 0.3, \phi_L = 2.0$ in this paper, let μ_S vary from -1 to 1, and ϕ_S varies from 0 to 2π. The $|\cos\iota|$ is presented in Fig. 5. We denote $\cos\iota = 1$ as the face-on case, $\cos\iota = -1$ as the face-off case, and $\cos\iota = 0$ is the edge-on case. Then we investigate the effect of sources' location and higher harmonics on SNRs, which are shown in Fig. 6.

Moreover, we show the effect of source location (μ_S, ϕ_S) on SNRs in Fig. 6 as well. The sources are still located at $z = 1$, with $m_1 = 10^6 M_\odot$, $m_2 = 10^5 M_\odot$, $\mu_L = 0.3$, $\phi_L = 2.0$, $\phi_c = 0$, $t_c = 0$ s, μ_S varies from -1 to 1, and ϕ_S varies from 0 to 2π (all information has been shown in Table I). Here, we only show the SNR results from the scenario that only includes the (2,2) mode. The SNRs for this particular scenario are approximately 10^2–10^3. Note that the loudest area is not the face-on or face-off areas, but slightly offset. When we consider a face-on or face-off binary system, indeed, $\tilde{h}_+(f)$ and $\tilde{h}_\times(f)$ reach their maximum values. However, it does not mean that $\tilde{h}(f)$ reaches its maximum value as well because of the different pattern functions. Furthermore, the SNRs in the edge-on area are much smaller, only about 10% of the loudest areas. This substantial SNR difference will lead to better parameter extraction near the face-on and face-off areas than at the edge-on areas, where the higher modes are prominent. Additionally, we have also investigated the results with different binary masses, which are consistent with the behaviors in Fig. 6, and we do not show them here.

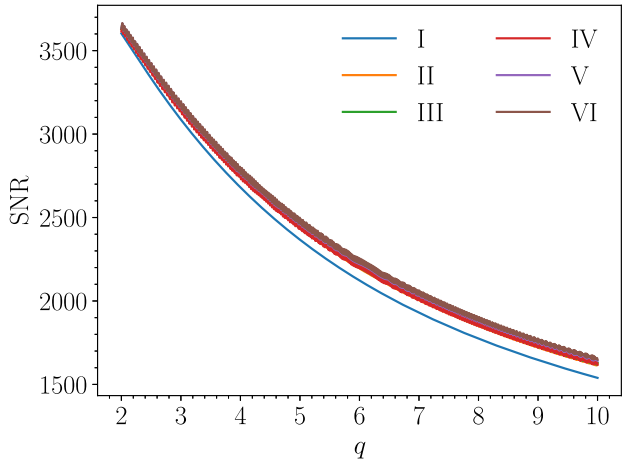

FIG. 4. The SNRs as a function of mass ratio q. The sources' parameters are the same as Fig. 3 except total mass $M = 1.1 \times 10^6 M_\odot$. Each curve corresponds to a different scenario and adopts the same notation as Fig. 3. Since we adopt a system with total mass $M = 1.1 \times 10^6 M_\odot$, the effect of higher harmonics modes is significant (cf. Fig. 2), so the oscillations of SNRs appear when incorporating higher harmonics.

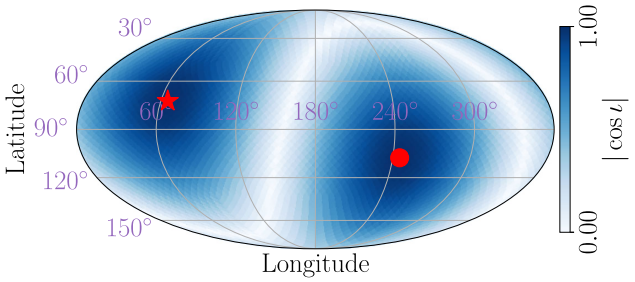

FIG. 5. The sky map of $|\cos\iota|$ in which $\mu_L = 0.3, \phi_L = 2.0$. The red star denotes $\cos\iota = 1$, i.e., the face-on case, and the red circle denotes $\cos\iota = -1$, i.e., the face-off case. We can see the edge-on cases as the white curve.

D. Parameter estimation

Bayesian inference is used to acquire the posterior distribution of the source parameters in GW transient data under the assumption that noise is Gaussian and stationary [14–17,58]. In principle, we should perform massive computational inference to obtain the posterior distribution of the binary parameters to investigate the higher harmonic effects. However, it seems to be improper to perform such a

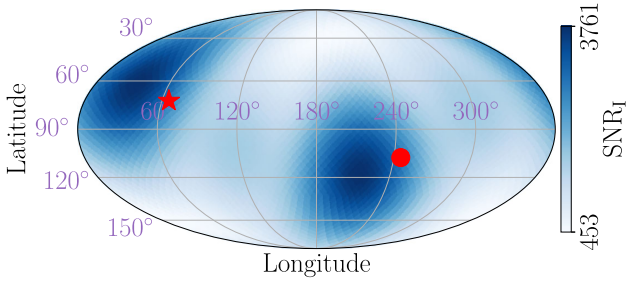

FIG. 6. The SNRs sky map of a binary with $m_1 = 10^6 M_\odot$, $m_2 = 10^5 M_\odot$, $z = 1$, and angular parameters $(\mu_S, \phi_S, \mu_L, \phi_L) = (-0.25, 2.31, 0.3, 2.0)$, where only the $(\ell, |m|) = (2, 2)$ mode is involved. The red star and red circle denote the face-on case and face-off cases, respectively.

task. Thanks to the large SNR of most GW signals we considered,[1] the sufficient and computationally cheap method, the Fisher information matrix [55,61], can be easily employed to estimate the parameters of the sources.

To demonstrate how to use the Fisher matrix, we use $\boldsymbol{\mathcal{P}}$ to denote the set of these parameters, and $\hat{\boldsymbol{\mathcal{P}}}$ to denote the parameters set that maximizes the likelihood function Λ, where

$$\Lambda = \exp\left[(\tilde{d}(f)|\tilde{h}(f)) - \frac{1}{2}(\tilde{h}(f)|\tilde{h}(f))\right], \tag{18}$$

where $\tilde{d}(f)$ is the Fourier transform result of $d(t)$ and $d(t)$ is the strain detected in the detector. Given the strain $d(t)$, the probability density function of the physical parameters $\boldsymbol{\mathcal{P}}$ is [55,61]

$$p(\boldsymbol{\mathcal{P}}|d) \propto \exp\left[-\frac{1}{2}\sum_{i,j}\Gamma_{ij}\Delta\mathcal{P}^i\Delta\mathcal{P}^j\right], \tag{19}$$

where Γ_{ij} is the Fisher information matrix (the inverse of the covariance matrix) of $\Delta\boldsymbol{\mathcal{P}} = \boldsymbol{\mathcal{P}} - \hat{\boldsymbol{\mathcal{P}}}$. The elements of Γ_{ij} can be obtained by

$$\Gamma_{ij} = \left(\frac{\partial\tilde{h}(f;\boldsymbol{\mathcal{P}})}{\partial\mathcal{P}^i}\middle|\frac{\partial\tilde{h}(f;\boldsymbol{\mathcal{P}})}{\partial\mathcal{P}^j}\right). \tag{20}$$

For the detector LISA, there are two equivalent L-shaped detectors A and B, so we can obtain the final Fisher matrix by linear superimposing the individual Fisher matrix,

$$\Gamma_{ij} = \Gamma^A_{ij} + \Gamma^B_{ij}. \tag{21}$$

For the parameters $\{\ln D_{\rm L}, t_c, \phi_0\}$, we can yield the analytic partial derivatives of them directly,

$$\frac{\partial\tilde{h}}{\partial\ln D_{\rm L}} = -\tilde{h}, \tag{22}$$

$$\frac{\partial\tilde{h}}{\partial t_c} = \mathrm{i}2\pi f\tilde{h}, \tag{23}$$

$$\frac{\partial\tilde{h}}{\partial\phi_0} = \mathrm{i}\sum_{\ell,m} m(F^+\mathcal{Y}^+_{\ell m} + F^\times\mathcal{Y}^\times_{\ell m})\tilde{h}_{\ell m}e^{-\mathrm{i}\phi_D}. \tag{24}$$

For the angular parameters, $\{\mu_S, \mu_L, \phi_S, \phi_L\}$, we can use the chain rule to obtain their analytic partial derivatives. However, their derivatives are too lengthy and uninspiring, so we do not show them here.

[1]Note that, the Fisher matrix method is only valid in the linear signal approximation (or high-SNR approximation). More details can be found in Refs. [59,60].

For the parameters $\mathcal{M}$ and η, we use central difference method to gain their derivatives,

$$\frac{\partial\tilde{h}(f;\boldsymbol{\mathcal{P}})}{\partial\mathcal{P}^i} \simeq \frac{\tilde{h}(f;\boldsymbol{\mathcal{P}} + \delta\mathcal{P}^i) - \tilde{h}(f;\boldsymbol{\mathcal{P}} - \delta\mathcal{P}^i)}{2\delta\mathcal{P}^i}. \tag{25}$$

To estimate the numerical error, we compare the result from the central difference method with that from JAX [62], a Python package performing the high-precision automatic differentiation algorithm to obtain the derivatives. The relative errors between our numerical method and JAX are under 1%.

III. RESULTS AND DISCUSSION

In this paper, we focus on the higher-harmonic effect on the parameter estimations of the chirp mass, symmetric mass ratio, luminosity distance, and sky location. Besides, we also investigate how the total mass M, mass ratio q, and source location impact the parameter estimations.

The angular resolution $\Delta\Omega$ can be expressed as [13,63]

$$\Delta\Omega = 2\pi\sqrt{(\Delta\mu_S\Delta\phi_S)^2 - [(\Gamma^{-1})_{\mu_S\phi_S}]^2}. \tag{26}$$

To make the results organized, we present effects from the total mass M and the mass ratio q in Sec. III A, and the impact of the sources' location in Sec. III B.

A. The effect of total mass and mass ratio

The effects of varying total mass M and higher-harmonic impact parameter estimation are illustrated in Fig. 7, which take the same sources' parameters as in Fig. 3. There exists an oscillatory behavior of SNRs (see Fig. 3). Such an oscillation is caused by the interference of each harmonic. In Fig. 7, a similar phenomenon reappears. This is because the parameters' variances are the diagonal elements of the $(\Gamma^{-1})_{ij}$, and Γ_{ij} are the inner product of waveform $\tilde{h}(f)$ derivatives. Meanwhile, the derivatives can be regarded as a linear superposition of each harmonic derivative since the $\tilde{h}(f)$ can be regarded as a linear superposition of each harmonic, which will lead to parameter extraction oscillation as M increases.

When higher harmonics are involved, the precisions on $\mathcal{M}$ and η increase by factors of $\sim$2 and $\sim$3 at most, respectively. As expected, the effect of higher harmonics becomes visible for $\mathcal{M}$ and η resolution with increasing M. The angular and $D_{\rm L}$ resolutions increase by factors of $\sim$3000 and $\sim$300 at most, respectively. Refer to Fig. 3; roughly speaking, the effect of higher harmonics beyond (3,3) can be neglected in this case, and a higher SNR means higher parameter estimation precision. However, Fig. 2 implies the higher harmonics are more significant for the heavier BBH. Our result shows significant improvement for $D_{\rm L}$ and Ω, as shown in Fig. 7, appears at $M \sim 10^6 M_\odot$,

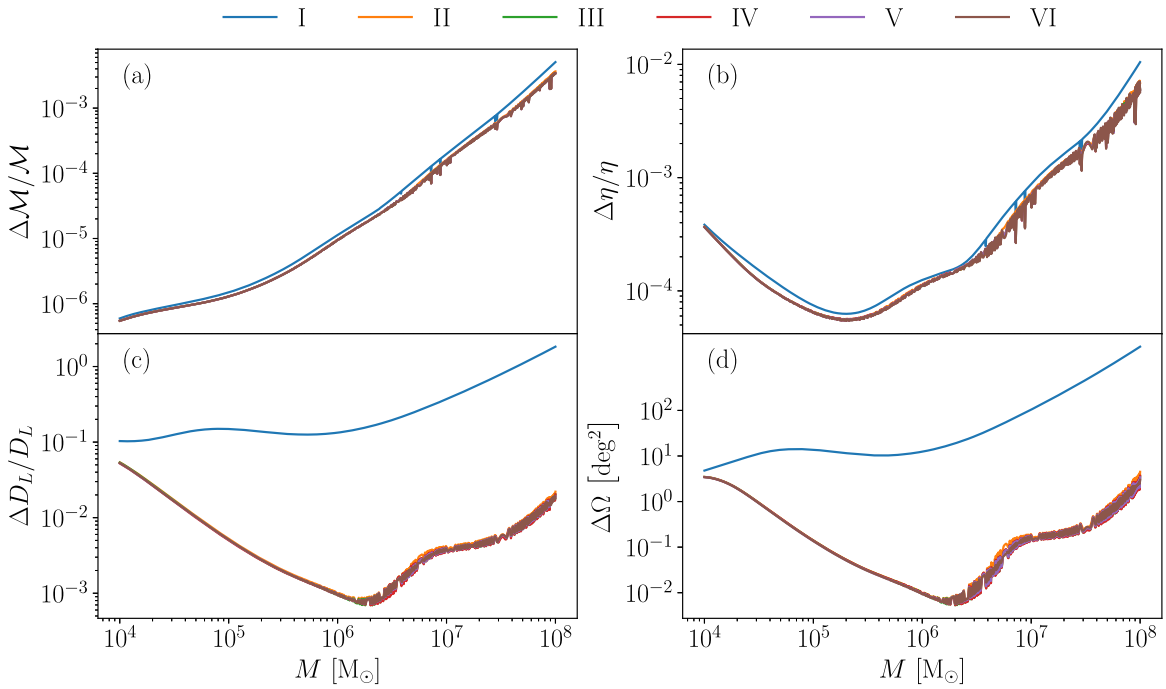

FIG. 7. The constraints on the chirp mass [panel (a)], the symmetric mass ratio [panel (b)], the luminosity distance [panel (c)], and the angular resolution [panel (d)] with the varying total mass M. We fix the mass ratio $q = 10$ and angular parameters $(\mu_S, \phi_S, \mu_L, \phi_L) = (-0.25, 2.31, 0.3, 2.0)$. Each curve represents a different scenario in Table. II.

where their merger frequencies correspond to the most sensitive frequency $\sim 2 \times 10^{-3}$ Hz for LISA.

In Fig. 7, we notice whether or not we are including higher modes into data analysis, the $\mathcal{M}$ and η estimations are highly precise. This is because the parameters $\mathcal{M}$ and η mainly contribute to the GW phase $\Phi(f)$, which can be detected at a highly precise level with a long-lived signal. As the M increases, the inspiral of the MBH binary becomes shorter, resulting in a decrease in precisions on $\mathcal{M}$, and η. In addition, the estimations of coalescence time t_c and ϕ_0 are also at a highly precise level for the same reason. However, for the inference of $D_{\rm L}$ and Ω, we mainly rely on two effects: one is the Doppler effect $\phi_D(\theta_S, \phi_S)$ [see Eq. (7)]; the other one is the LISA pattern factor functions $F^{+,\times}(\hat{\theta}_S, \hat{\phi}_S, \hat{\psi})$ [see Eq. (4)]. When the merger frequencies of MBH systems are in the most sensitive band of LISA, these GW features with higher modes will be well monitored by LISA. The interference of higher harmonics will be significant and easily be extracted from the data, resulting in breaking the $D_{\rm L}$-ι degeneracy, [see Eqs. (9) and (10)]. and reach a highly precise level.

Therefore, in Fig. 7, we will find that including higher harmonics only slightly affects $\mathcal{M}$ and η estimations but significantly impact $D_{\rm L}$ and Ω resolutions. Furthermore, it implies that the impact of including higher harmonics, for $D_{\rm L}$ and Ω resolution, is positively correlated to SNRs. This is the result that demonstrates that, compared with higher-harmonic itself, the higher-harmonics effect is more significant with the larger SNRs.

We also show the effects of varying mass ratio q and higher harmonics in Fig. 8, which takes the same sources' parameters as in Fig. 4. Similar to Fig. 7, whether or not we are including higher modes into data analysis, the estimations for $\mathcal{M}$ and η estimations are similar for the different scenarios, which are at the order 10^{-5} and 10^{-4}, respectively. However, the resolutions of $D_{\rm L}$ and Ω are at the order of 10% and 10 deg^2 precisions with only the (2,2) mode, respectively. When including higher modes, even with only the (3,3) mode, the estimations for $D_{\rm L}$ and Ω are improved massively. The results are consistent with the studies for varying M.

Refer to Fig. 4, the oscillation is significant, and a similar phenomenon reappears. Figure 8 shows the increases of $\mathcal{M}$ and η resolutions are tiny (a factor of $\sim$1.2 at most) when incorporating the higher harmonics. The angular and $D_{\rm L}$ resolutions increase dramatically by factors of $\sim 10^3$ and $\sim 10^2$ at most, respectively. Meanwhile, the increase in q leads to less improvement for the angular and $D_{\rm L}$ resolution since SNRs decrease. In addition to the (3,3) mode, we find that the (4,4) mode also has a slight impact on parameter extraction [see Fig. 8(b)]. This also is implied in Fig. 7 but is not significant.

In other words, the higher harmonics slightly affect $\mathcal{M}$ and η resolutions but impact dramatically on $D_{\rm L}$ and Ω resolutions. And the larger SNRs mean a better $D_{\rm L}$ and Ω resolution improvement. This is to be expected as we explained for Fig. 7.

In addition, Baibhav *et al.* [33] found that the errors of $D_{\rm L}$ and ι will diverge at $q \simeq 4$. This is because they used the

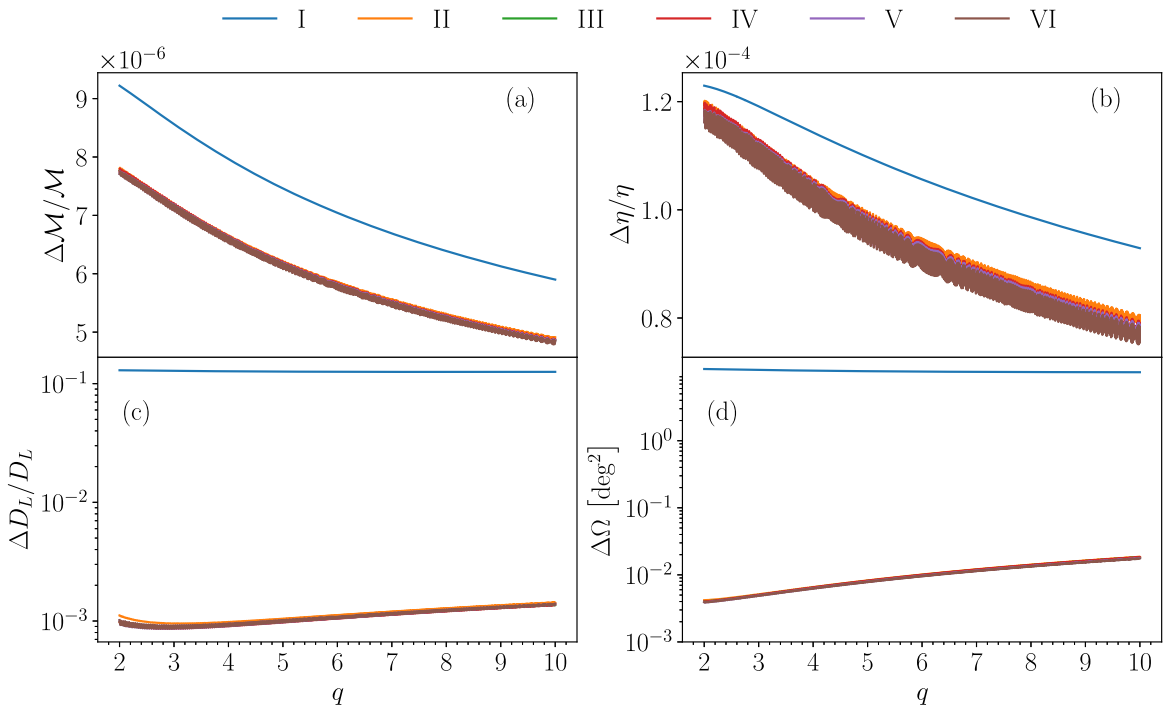

FIG. 8. Same as Fig. 7 with the varying mass ratio q. We fix the total mass $1.1 \times 10^6 M_\odot$.

analytic MBH ringdown waveform to estimate the parameters, whereas we use the full waveform.

B. The effect of source location

The impact of the sources' location is illustrated in Figs. 9 and 10. We do not show the sky maps for scenarios III–VI because the results of them are similar to scenario II.

Figure 9 shows the $\mathcal{M}$ and η resolution based on the $(\ell, |m|) = (2, 2)$ mode only (denoted with I as indicated in Table II) and the effect of the $(\ell, |m|) = (3, 3)$ mode (denoted with II as indicated in Table II). The sources' parameters are the same as Fig. 6. We find that in scenario I, the $\mathcal{M}$ and η resolutions are precise, at the order of 10^{-4}. Furthermore, in the face-on and face-off areas, the

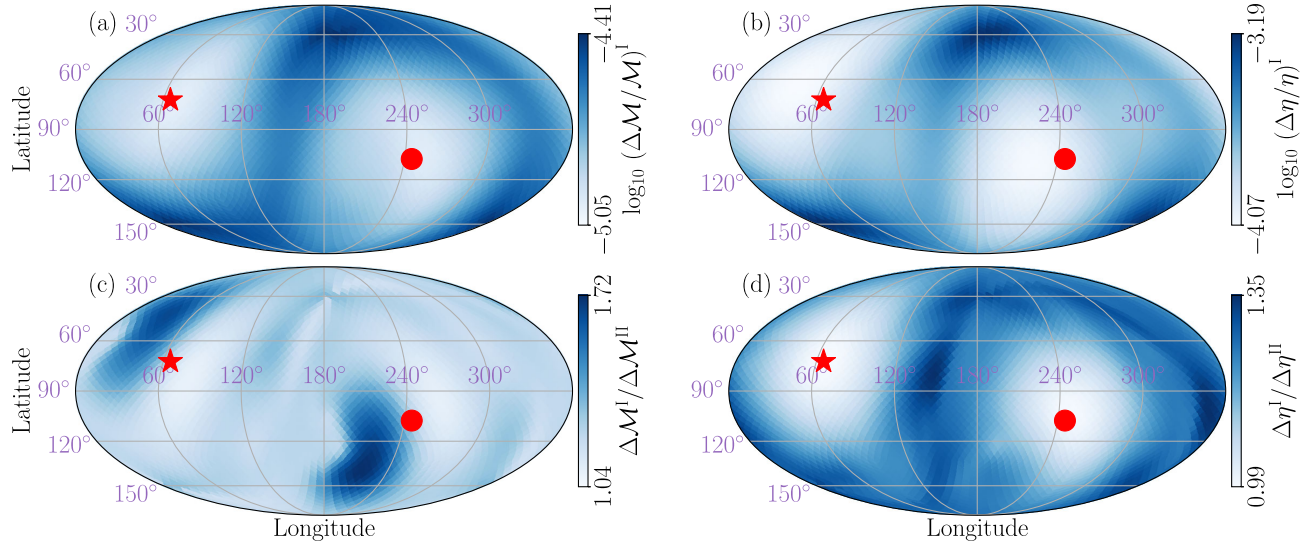

FIG. 9. The skymaps of $\mathcal{M}$ and η resolutions for the binary systems with the same source parameters as Fig. 6. The superscripts I and II denote the different scenarios in Table II. The top panel shows $\log_{10}(\Delta M/M)^{\mathrm{I}}$ [panel (a)] and $\log_{10}(\Delta\eta/\eta)^{\mathrm{I}}$ [panel (b)] which are only incorporating the (2,2) harmonic mode, and the bottom panel shows $\Delta M^{\mathrm{I}}/\Delta M^{\mathrm{II}}$ [panel (c)] and $\Delta\eta^{\mathrm{I}}/\Delta\eta^{\mathrm{II}}$ [panel (d)], the ratio of scenario I to scenario II for $\mathcal{M}$ and η resolutions. The red star and red circle denote the face-on case and face-off case, respectively.

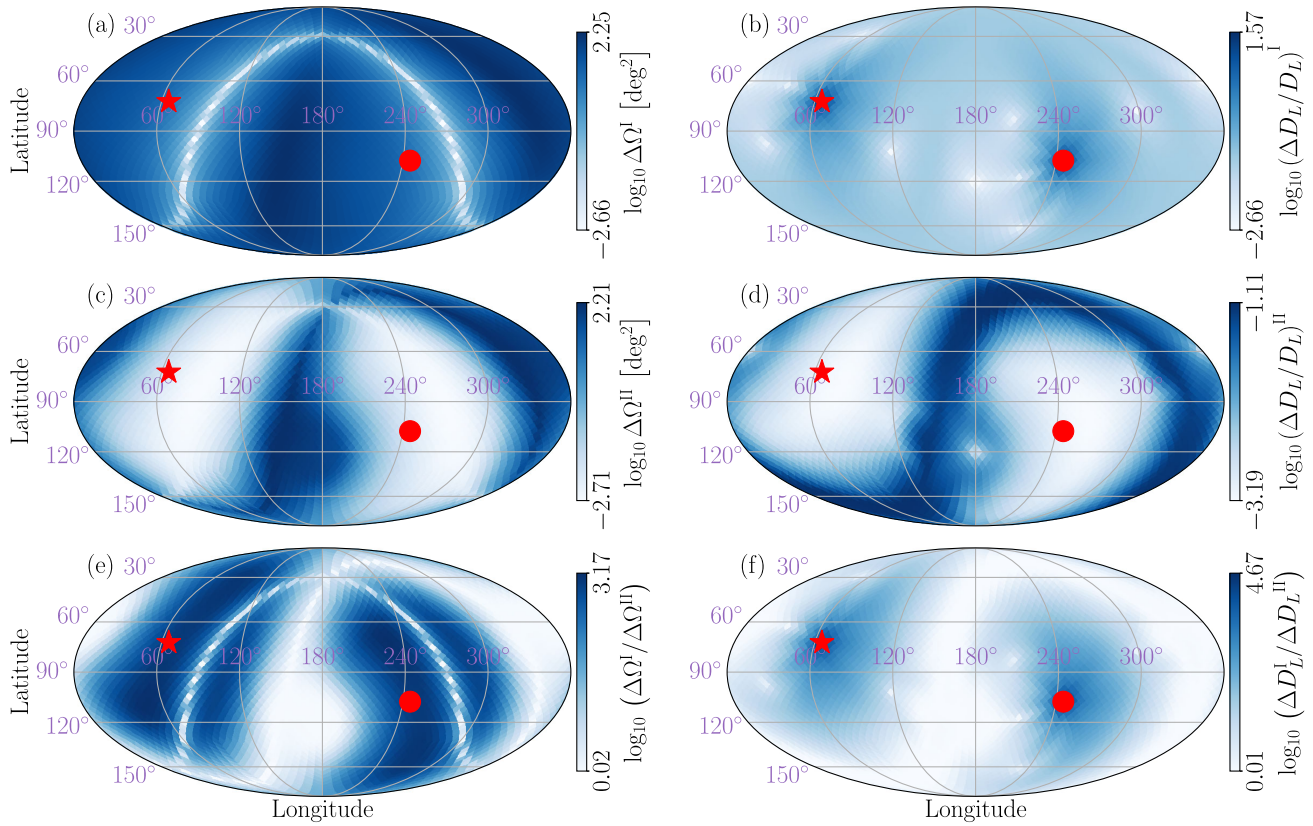

FIG. 10. Same as Fig. 9, but for angular and luminosity distance resolution, Ω and $D_{\rm L}$. The top panel shows $\log_{10}\Delta\Omega^{I}$ [panel (a)] and $\log_{10}(\Delta D_{\rm L}/D_{\rm L})^{\rm I}$ [panel (b)], i.e. the logarithmic Ω and $D_{\rm L}$ resolution of scenario I. The middle panel shows $\log_{10}\Delta\Omega^{\rm II}$ [panel (c)] and $\log_{10}(\Delta D_{\rm L}/D_{\rm L})^{\rm II}$ [panel (d)], the logarithmic resolutions of scenario II. The bottom panel shows $\log_{10}(\Delta\Omega^{\rm I}/\Delta\Omega^{\rm II})$ [panel (e)] and $\log_{10}(\Delta {\rm D}_{\rm L}^{\rm I}/\Delta {\rm D}_{\rm L}^{\rm II})$ [panel (f)], the logarithmic ratio of scenario I to scenario II for both Ω and $D_{\rm L}$ resolutions.

resolution is better than the edge-on area by factors of ∼4 and ∼8 for $\mathcal{M}$ and η, respectively. The better resolution of the face-on and face-off area is due to the larger SNR in this area. When the (3,3) mode is involved, the $\mathcal{M}$ resolution can be improved by up to ∼1.7, but in most regions, there is no improvement. The η resolution can be improved by up to ∼1.4. As expected, the improvement caused by including higher harmonics for the $\mathcal{M}$ and η resolution is marginal. To clarify, we have listed the probabilities of precision improvement in Table III, with the source parameters consistent with Fig. 6. The inclusions of higher modes do not significantly improve the precisions of these two parameters, $\mathcal{M}$ and η. Overall, we cannot expect a huge improvement in estimating $\mathcal{M}$ and η by considering higher harmonics. Nevertheless, if only considering the (2,2) mode, the degeneracy among parameters in the Fisher matrix is very strong near the face-on and face-off area, but higher harmonics will break it. Even if we consider the face-on or face-off MBH systems that theoretically do not contain higher modes (see Fig. 1), the inclusion of higher modes can help us better parameter estimations as well. In other words, the absence of a particular piece of information (mode) is also information in the data analysis.

We also illustrate the angular and luminosity distance resolution of scenario I and the $(\ell, |m|) = (3, 3)$ mode effect in Fig. 10. The inclusion of the $(\ell, |m|) = (3, 3)$ mode results in a dramatic increase in resolution in most

TABLE III. Probability of the typical value of improvements for chirp mass ($\mathcal{M}$) and symmetric mass ratio (η) by including higher harmonics compared with scenario I.

Improvement	1.2 (%)	1.4 (%)	1.6 (%)	1.8 (%)
$\mathcal{M}$				
II	77.83	12.21	3.12	0
III	86.36	14.71	4.52	0
IV	86.62	14.81	4.59	0
V	87.11	15.46	4.79	0
VI	87.34	15.33	4.85	0
η				
II	54.07	0	0	0
III	67.12	26.33	0	0
IV	67.51	28.78	0	0
V	68.23	35.84	0	0
VI	69.08	33.60	0	0

areas except for the near edge-on areas, as which can be foreseen from Figs. 7 and 8. The Ω and D_L resolutions can be improved by factors $\sim 10^3$ and $\sim 10^5$, respectively. Even though the inclusion of the (3,3) mode can significantly increase the angular resolution in most areas, the most sensitive resolution of scenario II is almost the same as scenario I. In other words, the (3,3) mode significantly improves the resolution where scenario I is poor. Nevertheless, the degeneration between parameters is strong near the face-on and face-off areas, and we take the results as an optimistic case.

While the D_L resolution improvement can reach a factor of 10^4, which is more than 10 times better than Ω resolution improvement, Fig. 10 indicates the improvement in Ω resolution is more promising. To better address it, we list the probability of the typical value for precision improvements in Table IV. The sources' parameters are consistent with Fig. 6 since it comes from Fig. 10. Besides the (3,3) mode, the (4,4) mode contributes the most to the precision improvement, and other higher harmonics contribute only slightly. Half of the D_L resolution improvements exceed 10, with approximately 3% surpassing over 10^3. For the angular resolution, over 70% of the improvements exceed 10, with around 10% surpassing over 10^3. Apart from the (3,3) mode, the other modes also have a slight effect, particularly when it comes to angular resolution.

C. The implication for the dark sirens

In Sec. III B, we show the improvement of the angular and luminosity distance resolution by including higher harmonics. These improvements can greatly enhance the probability of identifying the host galaxy of MBH. Meanwhile, such a dramatic improvement will substantially reduce the error caused by D_L in constraining H_0 and probe cosmology.

The localization of MBH can be mainly searched through the dark siren with the information of host galaxies. However, usually, the information derived from parameter estimation is not enough to identify them.

To investigate the probability of precise source localization, we define the volume $\Delta\mathcal{V}$ by

$$\Delta\mathcal{V} \simeq \Delta\Omega \frac{\Delta D_L}{D_L} D_L^3. \tag{27}$$

Here, $\Delta\mathcal{V}$ denotes the uncertainty volume of the host galaxies' location. With the assumption that the host galaxies are homogeneous and isotropic, the host galaxy can be identified in the threshold volume, and then the probability of identifying the host galaxy can be regarded as a function of the threshold volume, i.e. the probability that $\Delta\mathcal{V}$ is smaller than the threshold volume. Note that the average number density of the Milky-Way-like galaxy is ~ 0.01 Mpc^{-3} [64–66]. Therefore, the expected number of host galaxies in the threshold volume can be roughly estimated by $\Delta\mathcal{V} \times 0.01$ Mpc^{-3}. The probability is presented in Fig. 11 for the same sources' parameter as Fig. 6.

Figure 11 shows that the inclusion of the (3,3) mode will substantially enhance the probability of identifying the host galaxy, and the (4,4) mode contributes a visible improvement on this basis, while the rest modes do not. If the threshold is 10^{-2} Gpc^3 (the expected number of host galaxies is 10^5), considering only the (2,2) mode, the probability of identifying the host galaxy ∼8%, while considering higher harmonics, is over 70%. When the threshold is 10^{-4} Gpc^3 (the expected number of host galaxies is 10^3), the probability is ∼7% if only considering the (2,2) mode, while including higher harmonics it is over

TABLE IV. Same as Table III, but for luminosity distance (D_L) and angular resolution (Ω).

Improvement	10 (%)	10^2 (%)	10^3 (%)	10^4 (%)
D_L				
II	47.62	20.08	3.39	0.26
III	51.13	21.81	3.45	0.26
IV	51.36	21.48	3.35	0.26
V	52.70	21.45	3.48	0.26
VI	51.53	21.29	3.48	0.26
Ω				
II	68.35	46.03	8.56	0
III	71.97	50.39	9.67	0
IV	72.33	50.39	9.05	0
V	73.50	51.66	10.12	0
VI	72.43	50.81	10.32	0

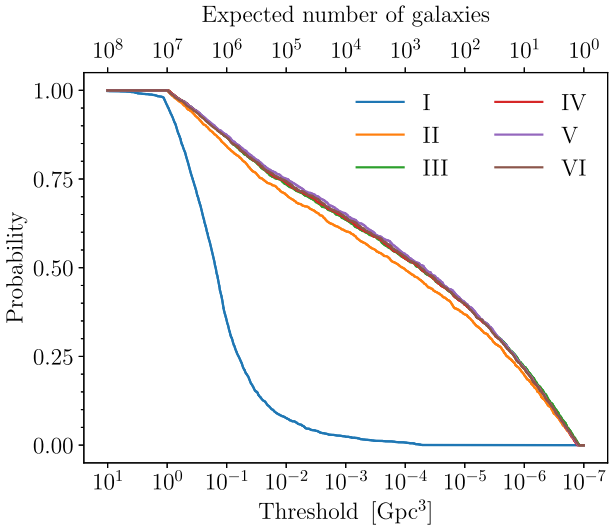

FIG. 11. The probability of identifying the host galaxy as a function of the threshold volume for the same parameters as in Fig. 6. Each curve corresponds to a different scenario, which is consistent with Table II. The top axis represents the expected number of host galaxies within the threshold volume, given an assumed number density of galaxies of 0.01 Mpc^{-3}.

50%. Even if the threshold is 10^{-6} Gpc^3 (the expected number of host galaxies is 10), the probability is around 20% if higher harmonics are involved. The (3,3) mode is vital for helping identify the host galaxy, while the (4,4) mode contributes slightly, and the other higher harmonics can be omitted in this sense. Moreover, the precise location is also helpful for early warning and EM counterparts' search. Thus, it is necessary to include the (3,3) mode at least into GW data analysis for MBH systems.

IV. CONCLUSION

BH in the Universe is the window to its host and the key to the treasure chest of cosmology. In this paper, we investigate the impact of various parameters such as mass, mass ratio, and source location. Moreover, we highlight the significant effect of higher harmonics on parameter estimation. The (3,3) mode is the most significant subdominant mode of GWs, the (4,4) mode has a slight effect on parameter extraction, and the other higher harmonics can be omitted for LISA.

The main conclusions are summarized in the following,

(i) For face-on or face-off MBH systems, in principle, their GW waveforms can be regarded almost as a (2,2)-mode composition (see Fig. 1). However, the inclusion of the (3,3) mode is still necessary for these systems to break the degeneracy in the parameter estimation. The information about the absence of a particular mode also contributes to the parameter estimation.

(ii) Including the (3,3) mode in the data analysis only has a slight effect on the $\mathcal{M}$ and η estimation. The improvements for those parameters are more related to the SNRs other than the inclusion of higher modes. Specifically, including the (3,3) mode leads to the measurements of $\mathcal{M}$ and η improved by a factor $\sim$2, roughly.

(iii) Including the (3,3) mode in data analysis significantly affects the $D_{\rm L}$ and Ω estimation. Including the (3,3) mode causes improvements in most of the 10^3 times in angular resolution and 10^4 times in luminosity distance resolution. When fixed, the redshift $z = 1$, relative to the (2,2) mode only, the precisions on luminosity distance and angular resolution from 50% MBH binary systems are improved by factors of 10 and 10^2, respectively.

(iv) Including the (3,3) mode will dramatically enhance the probability of source localization. When the threshold volume is 10^{-2} Gpc^3 (the expected number of host galaxies is 10^5), including the (3,3) mode will raise the probability up to 70%, while it will be less than 8% when only considering the (2,2) mode.

Higher harmonics have a great performance in extracting $D_{\rm L}$ and Ω. The great improvement in source localization may constrain H_0 precisely to arbitrate the existing H_0 tension problem. GWs emitted from CBCs are proposed as "sirens" to probe H_0. To precisely probe the H_0, precise $D_{\rm L}$ and source localization are vital. $D_{\rm L}$ inference is directly from GWs, and source localization is for identifying the host galaxy and obtaining z. However, the "standard sirens" are relatively rare in the Universe, which will limit the effect on probing H_0. Besides, the "dark sirens" will face the degeneration between parameters, which typically becomes severe near the face-on and face-off areas. This will significantly weaken the effect of probing H_0 by the dark sirens. Therefore, the H_0 measurement by "sirens" is not precise enough at present, and even the number of detected dark sirens is nearer to 2 orders of magnitude than that of standard sirens. For now, the contribution of constraining H_0 is dominated by only one standard siren, GW170817 [49,67].

Our study focuses on the effect of higher harmonics. We find the effect of the (3,3) mode is the most significant and leads to a significant improvement in the inferring source localization, which may identify the unique host galaxy of the dark sirens. Thus it may play a pivotal role in black hole physics, astronomy, and cosmology. Moreover, our analysis can be applied to other similar space-borne GW detectors, such as Taiji [68], TianQin [69], and DECIGO [70]. In the future, we expect that the inclusion of eccentricity and precession may enhance breaking degeneration further and increase the probability of identifying the host galaxies. Multiband and multidetector analysis may also have a visible effect.

ACKNOWLEDGMENTS

We thank the anonymous referee for constructive comments that improved the work. This work was supported in part by the National Key Research and Development Program of China Grant (No. 2021YFC2203001) and in part by the National Natural Science Foundation of China (Grants No. 11920101003, No. 12021003, No. 12005016, No. 12147177, No. 11975027, and No. 11991053). J. Z. is supported by the "LiYun" Postdoctoral Fellowship of Beijing Normal University. Z. Cao is supported by "the Interdiscipline Research Funds of Beijing Normal University" and CAS Project for Young Scientists in Basic Research YSBR-006. Y. Gong is supported by China Scholarship Council (CSC). L. S. is supported by the National SKA Program of China (2020SKA0120300) and the Max Planck Partner Group Program funded by the Max Planck Society.

[1] M. Volonteri, Formation of supermassive black holes, Astron. Astrophys. Rev. **18**, 279 (2010).

[2] J. Kormendy and L. C. Ho, Coevolution (or not) of supermassive black holes and host galaxies, Annu. Rev. Astron. Astrophys. **51**, 511 (2013).

[3] T. Alexander, Stellar dynamics and stellar phenomena near a massive black hole, Annu. Rev. Astron. Astrophys. **55**, 17 (2017).

[4] L. Barack *et al.*, Black holes, gravitational waves and fundamental physics: A roadmap, Classical Quantum Gravity **36**, 143001 (2019).

[5] B. F. Schutz, Determining the Hubble constant from gravitational wave observations, Nature (London) **323**, 310 (1986).

[6] D. E. Holz and S. A. Hughes, Using gravitational-wave standard sirens, Astrophys. J. **629**, 15 (2005).

[7] K. G. Arun *et al.* (LISA Collaboration), New horizons for fundamental physics with LISA, Living Rev. Relativity **25**, 4 (2022).

[8] J.-B. Bayle, B. Bonga, C. Caprini, D. Doneva, M. Muratore, A. Petiteau, E. Rossi, and L. Shao, Overview and progress on the laser interferometer space antenna mission, Nat. Astron. **6**, 1334 (2022).

[9] P. Amaro-Seoane *et al.* (LISA Collaboration), Laser interferometer space antenna, arXiv:1702.00786.

[10] J. Aasi *et al.* (LIGO Scientific Collaboration), Advanced LIGO, Classical Quantum Gravity **32**, 074001 (2015).

[11] F. Acernese *et al.* (Virgo Collaboration), Advanced Virgo: A second-generation interferometric gravitational wave detector, Classical Quantum Gravity **32**, 024001 (2015).

[12] T. Akutsu *et al.* (KAGRA Collaboration), Overview of KAGRA: Calibration, detector characterization, physical environmental monitors, and the geophysics interferometer, Prog. Theor. Exp. Phys. **2021**, 05A102 (2021).

[13] C. Cutler, Angular resolution of the LISA gravitational wave detector, Phys. Rev. D **57**, 7089 (1998).

[14] B. P. Abbott *et al.* (LIGO Scientific and Virgo Collaborations), GWTC-1: A Gravitational-Wave Transient Catalog of Compact Binary Mergers Observed by LIGO and Virgo during the First and Second Observing Runs, Phys. Rev. X **9**, 031040 (2019).

[15] R. Abbott *et al.* (LIGO Scientific and Virgo Collaborations), GWTC-2: Compact Binary Coalescences Observed by LIGO and Virgo During the First Half of the Third Observing Run, Phys. Rev. X **11**, 021053 (2021).

[16] R. Abbott *et al.* (LIGO Scientific and Virgo Collaborations), GWTC-2.1: Deep extended catalog of compact binary coalescences observed by LIGO and Virgo during the first half of the third observing run, arXiv:2108.01045 [Phys. Rev. D (to be published)].

[17] R. Abbott *et al.* (LIGO Scientific, Virgo, and KAGRA Collaborations), GWTC-3: Compact Binary Coalescences Observed by LIGO and Virgo During the Second Part of the Third Observing Run, arXiv:2111.03606 [Phys. Rev. X (to be published)].

[18] E. Berti, A. Buonanno, and C. M. Will, Estimating spinning binary parameters and testing alternative theories of gravity with LISA, Phys. Rev. D **71**, 084025 (2005).

[19] K. S. Thorne, Multipole expansions of gravitational radiation, Rev. Mod. Phys. **52**, 299 (1980).

[20] L. Blanchet, Gravitational radiation from post-Newtonian sources and inspiralling compact binaries, Living Rev. Relativity **17**, 2 (2014).

[21] L. London, S. Khan, E. Fauchon-Jones, C. García, M. Hannam, S. Husa, X. Jiménez-Forteza, C. Kalaghatgi, F. Ohme, and F. Pannarale, First Higher-Multipole Model of Gravitational Waves from Spinning and Coalescing Black-Hole Binaries, Phys. Rev. Lett. **120**, 161102 (2018).

[22] R. Abbott *et al.* (LIGO Scientific and Virgo Collaborations), GW190412: Observation of a binary-black-hole coalescence with asymmetric masses, Phys. Rev. D **102**, 043015 (2020).

[23] R. Abbott *et al.* (LIGO Scientific and Virgo Collaborations), GW190814: Gravitational waves from the coalescence of a 23 solar mass black hole with a 2.6 solar mass compact object, Astrophys. J. Lett. **896**, L44 (2020).

[24] K. Chatziioannou *et al.*, On the properties of the massive binary black hole merger GW170729, Phys. Rev. D **100**, 104015 (2019).

[25] N. V. Krishnendu and F. Ohme, Interplay of spin-precession and higher harmonics in the parameter estimation of binary black holes, Phys. Rev. D **105**, 064012 (2022).

[26] R. Wang and B. Hu, LitePIG: A lite parameter inference system for the gravitational wave in the millihertz band, Commun. Theor. Phys. **75**, 075402 (2023).

[27] Q. Gao, Y. You, Y. Gong, C. Zhang, and C. Zhang, Testing alternative theories of gravity with space-based gravitational wave detectors, Phys. Rev. D **108**, 024027 (2023).

[28] V. Varma and P. Ajith, Effects of nonquadrupole modes in the detection and parameter estimation of black hole binaries with nonprecessing spins, Phys. Rev. D **96**, 124024 (2017).

[29] V. Varma, S. E. Field, M. A. Scheel, J. Blackman, L. E. Kidder, and H. P. Pfeiffer, Surrogate model of hybridized numerical relativity binary black hole waveforms, Phys. Rev. D **99**, 064045 (2019).

[30] E. K. Porter and N. J. Cornish, The effect of higher harmonic corrections on the detection of massive black hole binaries with LISA, Phys. Rev. D **78**, 064005 (2008).

[31] M. Trias and A. M. Sintes, LISA observations of supermassive black holes: Parameter estimation using full post-Newtonian inspiral waveforms, Phys. Rev. D **77**, 024030 (2008).

[32] K. G. Arun, B. R. Iyer, B. S. Sathyaprakash, S. Sinha, and C. Van Den Broeck, Higher signal harmonics, LISA's angular resolution and dark energy, Phys. Rev. D **76**, 104016 (2007); Phys. Rev. D **76**, 129903(E) (2007).

[33] V. Baibhav, E. Berti, and V. Cardoso, LISA parameter estimation and source localization with higher harmonics of the ringdown, Phys. Rev. D **101**, 084053 (2020).

[34] S. Marsat, J. G. Baker, and T. Dal Canton, Exploring the Bayesian parameter estimation of binary black holes with LISA, Phys. Rev. D **103**, 083011 (2021).

[35] G. Pratten, A. Klein, C. J. Moore, H. Middleton, N. Steinle, P. Schmidt, and A. Vecchio, On the LISA science performance in observations of short-lived signals from massive black hole binary coalescences, Phys. Rev. D **107**, 123026 (2023).

[36] M. L. Katz, Fully automated end-to-end pipeline for massive black hole binary signal extraction from LISA data, Phys. Rev. D **105**, 044055 (2022).

[37] K. K. Y. Ng *et al.*, Measuring properties of primordial black hole mergers at cosmological distances: Effect of higher order modes in gravitational waves, Phys. Rev. D **107**, 024041 (2023).
[38] F. Iacovelli, M. Mancarella, S. Foffa, and M. Maggiore, GWFAST: A Fisher information matrix Python code for third-generation gravitational-wave detectors, Astrophys. J. Suppl. Ser. **263**, 2 (2022).
[39] B. P. Abbott *et al.* (LIGO Scientific and Virgo Collaborations), GW170817: Observation of Gravitational Waves from a Binary Neutron Star Inspiral, Phys. Rev. Lett. **119**, 161101 (2017).
[40] D. A. Coulter *et al.*, Swope supernova survey 2017a (SSS17a), the optical counterpart to a gravitational wave source, Science **358**, 1556 (2017).
[41] B. P. Abbott *et al.* (LIGO Scientific, Virgo, Fermi-GBM, and INTEGRAL Collaborations), Gravitational waves and gamma-rays from a binary neutron star merger: GW170817 and GRB 170817A, Astrophys. J. Lett. **848**, L13 (2017).
[42] B. P. Abbott *et al.* (LIGO Scientific, Virgo, Fermi GBM, INTEGRAL, IceCube, AstroSat Cadmium Zinc Telluride Imager Team, IPN, Insight-Hxmt, ANTARES, Swift, AGILE Team, 1M2H Team, Dark Energy Camera GW-EM, DES, DLT40, GRAWITA, Fermi-LAT, ATCA, ASKAP, Las Cumbres Observatory Group, OzGrav, DWF (Deeper Wider Faster Program), AST3, CAASTRO, VINROUGE, MASTER, J-GEM, GROWTH, JAGWAR, CaltechNRAO, TTU-NRAO, NuSTAR, Pan-STARRS, MAXI Team, TZAC Consortium, KU, Nordic Optical Telescope, ePESSTO, GROND, Texas Tech University, SALT Group, TOROS, BOOTES, MWA, CALET, IKI-GW Follow-up, H.E.S.S., LOFAR, LWA, HAWC, Pierre Auger, ALMA, Euro VLBI Team, Pi of Sky, Chandra Team at McGill University, DFN, ATLAS Telescopes, High Time Resolution Universe Survey, RIMAS, RATIR, and SKA South Africa/MeerKAT Collaborations), Multi-messenger observations of a binary neutron star merger, Astrophys. J. Lett. **848**, L12 (2017).
[43] B. P. Abbott *et al.* (LIGO Scientific, Virgo, 1M2H, Dark Energy Camera GW-E, DES, DLT40, Las Cumbres Observatory, VINROUGE, and MASTER Collaborations), A gravitational-wave standard siren measurement of the Hubble constant, Nature (London) **551**, 85 (2017).
[44] N. Aghanim *et al.* (Planck Collaboration), Planck 2018 results. VI. Cosmological parameters, Astron. Astrophys. **641**, A6 (2020); Astron. Astrophys. **652**, C4(E) (2021).
[45] A. G. Riess *et al.*, A comprehensive measurement of the local value of the Hubble constant with 1 $\mathrm{km\,s^{-1}\,Mpc^{-1}}$ uncertainty from the Hubble space telescope and the SH0ES team, Astrophys. J. Lett. **934**, L7 (2022).
[46] M. Soares-Santos *et al.* (DES, LIGO Scientific, and Virgo Collaborations), First measurement of the Hubble constant from a dark standard siren using the dark energy survey galaxies and the LIGO/Virgo binary–black-hole merger GW170814, Astrophys. J. Lett. **876**, L7 (2019).
[47] A. Palmese *et al.* (DES Collaboration), A statistical standard siren measurement of the Hubble constant from the LIGO/Virgo gravitational wave compact object merger GW190814 and dark energy survey galaxies, Astrophys. J. Lett. **900**, L33 (2020).
[48] B. P. Abbott *et al.* (LIGO Scientific and Virgo Collaborations), A gravitational-wave measurement of the Hubble constant following the second observing run of Advanced LIGO and Virgo, Astrophys. J. **909**, 218 (2021).
[49] R. Abbott *et al.* (LIGO Scientific, Virgo, and KAGRA Collaborations), Constraints on the cosmic expansion history from GWTC-3, Astrophys. J. **949**, 76 (2023).
[50] A. Finke, S. Foffa, F. Iacovelli, M. Maggiore, and M. Mancarella, Cosmology with LIGO/Virgo dark sirens: Hubble parameter and modified gravitational wave propagation, J. Cosmol. Astropart. Phys. 08 (2021) 026.
[51] T. Yang, R.-G. Cai, Z. Cao, and H. M. Lee, Eccentricity of Long Inspiraling Compact Binaries Sheds Light on Dark Sirens, Phys. Rev. Lett. **129**, 191102 (2022).
[52] C. Liu, L. Shao, J. Zhao, and Y. Gao, Multiband observation of LIGO/Virgo binary black hole mergers in the gravitational-wave transient catalog GWTC-1, Mon. Not. R. Astron. Soc. **496**, 182 (2020).
[53] A. Buonanno, B. Iyer, E. Ochsner, Y. Pan, and B. S. Sathyaprakash, Comparison of post-Newtonian templates for compact binary inspiral signals in gravitational-wave detectors, Phys. Rev. D **80**, 084043 (2009).
[54] A. Buonanno, G. B. Cook, and F. Pretorius, Inspiral, merger and ring-down of equal-mass black-hole binaries, Phys. Rev. D **75**, 124018 (2007).
[55] L. S. Finn, Detection, measurement and gravitational radiation, Phys. Rev. D **46**, 5236 (1992).
[56] T. Robson, N. J. Cornish, and C. Liu, The construction and use of LISA sensitivity curves, Classical Quantum Gravity **36**, 105011 (2019).
[57] C. Mills and S. Fairhurst, Measuring gravitational-wave higher-order multipoles, Phys. Rev. D **103**, 024042 (2021).
[58] J. Veitch *et al.*, Parameter estimation for compact binaries with ground-based gravitational-wave observations using the LALInference software library, Phys. Rev. D **91**, 042003 (2015).
[59] M. Vallisneri, Use and abuse of the Fisher information matrix in the assessment of gravitational-wave parameter-estimation prospects, Phys. Rev. D **77**, 042001 (2008).
[60] J. Zhao, L. Shao, Y. Gao, C. Liu, Z. Cao, and B.-Q. Ma, Probing dipole radiation from binary neutron stars with ground-based laser-interferometer and atom-interferometer gravitational-wave observatories, Phys. Rev. D **104**, 084008 (2021).
[61] C. Cutler and É. E. Flanagan, Gravitational waves from merging compact binaries: How accurately can one extract the binary's parameters from the inspiral wave form?, Phys. Rev. D **49**, 2658 (1994).
[62] J. Bradbury, R. Frostig, P. Hawkins, M. J. Johnson, C. Leary, D. Maclaurin, G. Necula, A. Paszke, J. VanderPlas, S. Wanderman-Milne, and Q. Zhang, JAX: Composable transformations of Python + NumPy programs (2018), http://github.com/google/jax.
[63] L. Barack and C. Cutler, LISA capture sources: Approximate waveforms, signal-to-noise ratios, and parameter estimation accuracy, Phys. Rev. D **69**, 082005 (2004).
[64] R. K. Kopparapu, C. Hanna, V. Kalogera, R. O'Shaughnessy, G. González, P. R. Brady, and S. Fairhurst, Host galaxies

catalog used in LIGO searches for compact binary coalescence events, Astrophys. J. **675**, 1459 (2008).

[65] J. Abadie *et al.* (LIGO Scientific and Virgo Collaborations), Predictions for the rates of compact binary coalescences observable by ground-based Gravitational-wave detectors, Classical Quantum Gravity **27**, 173001 (2010).

[66] H.-Y. Chen and D. E. Holz, Finding the one: Identifying the host galaxies of gravitational-wave sources, arXiv:1612.01471.

[67] M. Bulla, M. W. Coughlin, S. Dhawan, and T. Dietrich, Multi-messenger constraints on the Hubble constant through combination of gravitational waves, gamma-ray bursts and kilonovae from neutron star mergers, Universe **8**, 289 (2022).

[68] Y.-L. Wu *et al.* (Taiji Scientific Collaboration), China's first step towards probing the expanding universe and the nature of gravity using a space borne gravitational wave antenna, Commun. Phys. **4**, 34 (2021).

[69] J. Luo *et al.* (TianQin Collaboration), TianQin: A space-borne gravitational wave detector, Classical Quantum Gravity **33**, 035010 (2016).

[70] S. Sato *et al.*, The status of DECIGO, J. Phys. Conf. Ser. **840**, 012010 (2017).